Mineralium Deposita (2023) 58:1317–1332
https://doi.org/10.1007/s00126-023-01184-w

ARTICLE

Genesis of No. 2 orebody of the Jinchuan magmatic Ni-Cu-(PGE) sulfide deposit, NW China: New constraints from the newly discovered deep extension

Ting-Mao Long[1,2] · Xie-Yan Song[1] · Jian Kang[1,2] · Qing-Lin Liang[1,2] · Yong-Cai Wang[3] · De-Xian Li[3] · Qi-Xing Ai[3] · Wen-De Suo[3] · Jian-Quan Lu[3]

Received: 15 July 2022 / Accepted: 3 June 2023 / Published online: 14 June 2023

Abstract

The world-class Jinchuan magmatic Ni-Cu-PGE (platinum-group element) sulfide deposit comprises four large orebodies (No. 1, 2, 3 and 24). Underground fan drilling discovered significant lateral extension of No. 2 orebody, referred as No. 2a in this study. From base to top, the No. 2a orebody comprises disseminated sulfide in olivine pyroxenites, net-textured ore in lherzolite, and massive ore. Despite different host rocks, the contents of Ni, Cu and PGE of the same types of sulfide ores from No. 2 and No. 2a orebodies are comparable. Mass balance calculation indicates that the parental magmas contained 0.01–0.05 ppb Ir and 0.2-0.8 ppb Pd, which are about one order of magnitude less than PGE abundances of undepleted continental flood basalts. PGE tenors (recalculated to 100% sulfides) of the net-textured ores from both orebodies increase upward. We attribute this to variations in magma:sulfide ratios of successive batches of recharged magmas and/or reaction of sulfides with less evolved magma. We propose that the No. 2a and No. 2 orebodies were located in the upstream and downstream parts of an originally sub-horizontal magma conduit, respectively. Sulfide liquids accumulated in the wider parts of the magma conduit to form No. 2a and No. 2 orebodies progressively. Variable locations within the intrusion and sharp contacts with other types of sulfide ore indicate that the massive ores formed by injection of pooled sulfide melt. Significant Pt-depletion of the massive ores and Pt enrichment in the adjacent net-textured ores suggest migration of residual fractionated sulfide liquids.

Keyword Jinchuan magmatic sulfide deposit · Newly discovered orebody · Platinum group elements · Ore forming processes

Introduction

The Jinchuan magmatic sulfide deposit is the world's third largest operating Ni-Cu-PGE mine after Noril'sk in Russia and Sudbury in Canada. Exploration in the 1960s at Jinchuan had delineated 5.4 million tonnes (Mt) Ni and 3.5 Mt Cu metals with an average grade of 1.06% and 0.7%, respectively (Sixth Geological Unit 1984). Several new orebodies that contain 0.85 Mt Ni and 0.5 Mt Cu in total had been discovered via underground prospecting programs in the past ten years at Jinchuan (from Jinchuan group Ltd).

Zircon U–Pb dating indicates that the intrusion was emplaced in the Neoproterozoic (827 ± 8 Ma, Li et al. 2005, 831 ± 0.6 Ma, Zhang et al. 2010). Negative $\varepsilon_{Nd(t)}$ values and high γ_{Os} values of the Jinchuan rocks as well as low Mn contents in the olivine suggest that the primary magma was derived from partial melting of a metasomatised mantle source (Li et al. 2005; Tonnelier 2010; Lu et al. 2019). There are four large orebodies in the Jinchuan intrusion. No. 3 and 24 orebodies are hosted in Segments I and III in the west, whilst No. 1 and 2 orebodies are hosted in Segments II and IV in the east (Fig. 1c) (Song et al. 2012). Distinguishable characteristics of the four orebodies in terms of their

Editorial handling: W. D. Maier

✉ Xie-Yan Song
songxieyan@vip.gyig.ac.cn

1 State Key Laboratory of Ore Deposit Geochemistry, Institute of Geochemistry, Chinese Academy of Sciences, Guiyang 550081, People's Republic of China

2 University of Chinese Academy of Sciences, Beijing 100049, People's Republic of China

3 State Key Laboratory of Nickel and Cobalt Resources Comprehensive Utilization, Jinchuan Group Ltd, Jinchuan, Gansu 737100, People's Republic of China

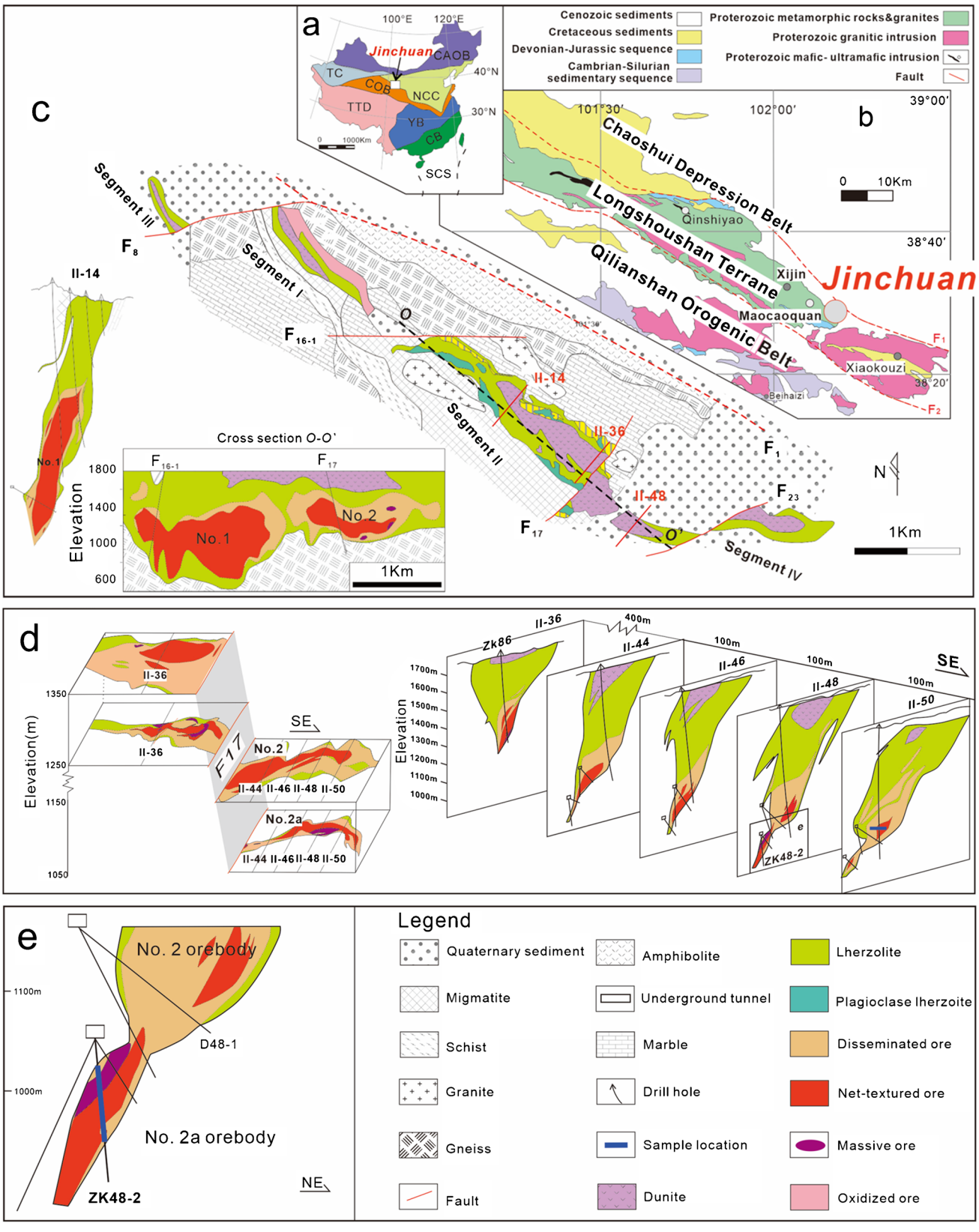
a
100°E
120°E
40°N
30°N
Jinchuan
CAOB
TC
COB
NCC
TTD
YB
CB
SCS
0 1000Km
Cenozoic sediments
Cretaceous sediments
Devonian-Jurassic sequence
Cambrian-Silurian sedimentary sequence
Proterozoic metamorphic rocks&granites
Proterozoic granitic intrusion
Proterozoic mafic- ultramafic intrusion
Fault
b
101°30′
102°00′
39°00′
38°40′
38°20′
Chaoshui Depression Belt
Longshoushan Terrane
Qilianshan Orogenic Belt
Qinshiyao
Xijin
Maocaoquan
Xiaokouzi
Beihaizi
Jinchuan
0 10Km
F1
F2
c
Segment III
Segment I
Segment II
Segment IV
F8
F16-1
F17
F23
O
O'
II-14
II-36
II-48
No.1
No.2
Cross section O-O'
Elevation
1800
1400
1000
600
1Km
N
d
Elevation(m)
1350
1250
1150
1050
II-36
SE
F17
No.2
II-44 II-46 II-48 II-50
No.2a
II-44 II-46 II-48 II-50
Elevation
1700m
1600m
1500m
1400m
1300m
1200m
1100m
1000m
Zk86
II-36
400m
II-44
100m
II-46
100m
II-48
100m
II-50
SE
ZK48-2
e
1100m
1000m
No. 2 orebody
D48-1
No. 2a orebody
ZK48-2
NE
Legend
Quaternary sediment
Migmatite
Schist
Granite
Gneiss
Fault
Amphibolite
Underground tunnel
Marble
Drill hole
Sample location
Dunite
Lherzolite
Plagioclase lherzoite
Disseminated ore
Net-textured ore
Massive ore
Oxidized ore

◂**Fig. 1** (**a**) Tectonic sketch of China showing location of North China Craton. (**b**) Simplified geological map of the Longshou terrane at southwestern margin of North China Craton (after Song et al. 2009, 2012). (**c**) Sketch of the Jinchuan intrusion and geological profile of Segment II and No.1 orebody (after Song et al. 2012); (**d**) Horizontal and vertical sections showing geological features of No. 2 orebody (from Jinchuan Company). (**e**) Cross-section of the newly discovered orebody (No. 2a orebody) beneath No. 2 orebody. Abbreviations: CAOB = Central-Asia Orogenic Belt, NCC = North China Craton, TC = Tarim Craton, COB = Central Orogenic Belt, TTD = Tibetan Tectonic Domain, YB = Yangtze Block, CB = Cathaysian Block, SCS = South China Sea

geology and geochemistry suggest that they may result from different sulfide segregation and concentration processes in separate branches of a magma conduit system (Song et al. 2009, 2012; Chen et al. 2013; Kang et al. 2022).

A series of drill holes reveal that the No. 1 and No. 2 orebodies are unconnected. They are situated in the western and eastern portions of Segment II, respectively (Song et al. 2009, 2012). A lensoid orebody extending downward from No. 2 orebody was found in 2016–2017 during an underground prospecting program. This newly discovered orebody has been named No. 2a and has average grades of 1.83% Ni and 0.93% Cu, respectively (Fig. 1e). In this study, the genetic linkage between No. 2 and No. 2a orebodies as well as the mechanism of ore segregation and deposition in the eastern portion of Segment II are demonstrated based on comparisons of petrographic features and Ni, Cu and PGE data. The new insights indicate that No. 2a orebody is the upstream of No. 2 orebody and there is still much exploration potential at depth.

Geological background

The Longshoushan terrane is located at the southwestern the margin of North China craton (Fig. 1a). Jinchuan is situated at the northern margin of the Longshoushan terrane, which is bounded by the NW-trending regional reverse faults F_1 and F_2 to the north and south (Fig. 1b). The terrane comprises mainly Proterozoic migmatite, gneiss, slate, and marble (Sixth Geological Unit 1984). A series of mafic–ultramafic intrusions (e.g., Jinchuan and Zangbutai) intruded into the Proterozoic metamorphic rocks. However, with the exception of Jinchuan, no economic Cu-Ni mineralization was recognized(Sixth Geological Unit 1984; Tang 1991; Tang and Li 1995; Barnes and Tang 1999).

The Jinchuan intrusion is divided by E-W trending strike-slip faults into Segments III, I, II and IV from the west to the east (Fig. 1c) (Song et al. 2012). Segment I and Segment III have two lithologic cycles. The upper cycle thickens to the west and consists of olivine-sulfide cumulate and disseminated sulfides in lherzolite and olivine pyroxenite (from base to top). The lower cycle thickens toward the east and contains sulfide-olivine cumulate, disseminated ore in lherzolite and olivine pyroxenite from the bottom up. Sharp contacts between the two cycles and field relationships indicate that the upper cycle formed earlier (Kang et al. 2022). The No. 3 and 24 orebodies developed in the lower parts of the upper and lower cycles, respectively (Song et al. 2012; Chen et al. 2013; Kang et al. 2022).

Segments II and IV, divided by the fault F_{23}, comprise mainly medium-fine-grained sulfide-olivine cumulate, sulfide-bearing or barren- lherzolite (Fig. 1c). The No. 1 orebody, extending from the western end to the middle part of Segment II, is ~ 1600 m long with an average thickness of ~ 90 m and dominantly composed of sulfide-olivine cumulate, which is enveloped by thin margins of disseminated ore in lherzolite (Fig. 1c) (Song et al. 2009). The No. 2 orebody is developed at the bottom of the eastern part of Segment II and extends to Segment IV. It is ~ 1300 m long and ~ 120 m thick on average. The orebody comprises sulfide-olivine cumulate at the base and disseminated ore in lherzolite in its upper portion (Fig. 1d). Lensoid or irregularly shaped bodies of massive ore (> 90 vol% sulfide) occur at the margins of, or within, the No. 2 orebody and may intrude into the barren lherzolite at a few locations. The massive ores have sharp contacts with the disseminated and/or net-textured ores and contain xenoliths of net-textured or disseminated ores and lherzolite (Fig. 1d, ESM Fig. 1). The largest massive ore lens is up to 200 m long and 20 m thick (Sixth Geological Unit 1984). The net-textured and disseminated ores contain 20–30 vol% and 5–10 vol% sulfides, respectively (ESM Fig. 2b-g) (Sixth Geological Unit 1984; Song et al. 2009).

The newly discovered No. 2a orebody is much smaller than the No. 2 orebody, being ~ 250 m long, up to 50 m thick, and comprising (from base to top) disseminated sulfide in olivine pyroxenite and net-textured sulfide in lherzolite (Fig. 1d). As shown in Fig. 1 e, a narrow connection between the orebodies No. 2 and No. 2a demonstrates that the latter is the extension of the No. 2 orebody. Previous studies on lithological relationships have attested that the Jinchuan intrusion was originally sub-horizontal before tectonic deformation (De Waal et al. 2004; Song et al. 2012). Thus, No. 2a orebody is referred to the lateral extension of the No. 2 orebody. The sulfide contents are less than 10 vol% and 15–30 vol% in the disseminated ores and net-textured ores of No. 2a, respectively (ESM Fig. 2d-g). It is noteworthy that patches of sulfides associated with olivine occur at the top of the net-textured ores (ESM Fig. 2d-f). A similar phenomenon was found in the No. 1 orebody by Tonnelier (2010). A ~ 100 m long massive ore lens (up to 20 m thick) consisting of > 90 vol% sulfide occurs above the net-textured ore with a sharp contact (Fig. 1d-e). The dominant sulfides in all of the mineralized zones are pyrrhotite, pentlandite and chalcopyrite (ESM Fig. 3). Anhedral magnetite occurs at the boundaries of the sulfides due to decomposition of pyrrhotite during

hydrothermal alteration (ESM Fig. 3e). Serpentinization of olivine also produced a combination of very fine grains of magnetite and serpentine along fractures. Euhedral magnetite grains are rare in the sulfide ores.

Sampling and analytical methods

Fifteen samples were collected from the underground drill core ZK48-2, which intersected the newly discovered orebody (Fig. 1e). Each sample was split off from 2 m long drill core and was crushed to small grains (< 5 mm in diameter) using a tungsten carbide ring mill. About 500 g of the crushed grains were milled to -200 mesh powder for geochemical analysis. For comparison, another 16 hand specimen were taken from a mining tunnel (at elevation of 1150 m) across the No. 2 orebody along exploration line II-50, which is near drill hole ZK48-2 (Fig. 1d). Each sample weighted more than 500 g and was crushed and milled to -200 mesh.

Analyses of oxides, Cu, Ni and S of the powders were completed at ALS Chemex (Guangzhou) Co. Ltd. Whole-rock oxide in the drill core samples were analyzed using a PANalytical Axios X-ray fluorescence spectrometer (XRF) on fused glass beads. Using the procedure described in detail by Xie et al. (2014) and Song et al. (2020). Copper and Ni in samples containing more than 1.0 vol% sulfides were measured using a Varian ICP735-ES inductively coupled plasma emission spectrometer and a Perkin Elmer Elan 9000 inductively coupled plasma mass spectrometer (ICP-MS), respectively. Whole-rock S were measured by Leco furnace and infrared (IR) absorption with detection limits of ~ 0.01 wt %. The analytical accuracy of oxides and S is ± 3% relative, whilst that of Ni and Cu is ± 2% relative. The analyses results are listed in ESM Table 1.

Analysis of PGE was conducted via isotope dilution (ID)-ICP-MS using an improved digestion technique at Institute of Geochemistry, Chinese Academy of Sciences. For the disseminated, net-textured, and massive ores,10 g, 5-8 g, and 2-5 g powders were weighted for analysis, respectively. The sample was digested using Teflon beakers sealed in a stainless-steel pressure bomb, and the solution was used to collect PGE by Te co-precipitation (Qi et al. 2011). The measured results of PGE for the reference materials UMT-1 and WPR-1 agree well with recommended values reported by Qi et al. (20042011). Analysis results of the samples and the standards are listed in ESM Table 2, results of the duplicates are within the error range.

Four massive ore samples from the drill-holes ZK86 and ZK48-2 were analyzed to assess nugget effects on PGE contents due to the possible existence of inhomogeneously distributed PGE minerals (e.g., sperrylite, irarsite). For example, sperrylite crystals larger than 75μmmay be stuck in the residuals during crushing and milling and may result in Pt depletion of the powder because sperrylite has Mohs hardness of 6–7, higher than pyrrhotite, pentlandite and chalcopyrite (3.5–4). Each massive ore sample weighting ~ 100 g was crushed with an agate mortar and pestle, and the crushed sample was sieved to obtain a part of 200-mesh powder. The residual crushed grains were then repeatedly crushed and sieved to make four parts of 200-mesh powder weighting 20–30 g for each sample. The PGE compositions of the powder splits were measured separately using the method described above. The analytical results are given in ESM Table 3.

Results

Major oxide compositions

The sulfide ores have LOIs of 3.4 to 14 wt% due to high percentages of sulfides and serpentinized olivine (ESM Table 1). Before plotting of binary diagrams and chemostratigraphic columns, the concentrations of major and trace elements have been recalculated to 100% on a volatile-free basis. Iron in sulfides is subtracted from the total on assumption of molar (Fe + Ni + Cu)/S ratio of 1:1 in the base-metal sulfides according to pyrrhotite, pentlandite and chalcopyrite molecular formulae.

The data suggest that the sulfide mineralized and unmineralized lherzolite in drill-hole ZK86, which cut through No. 2 orebody, have relatively constant $MgO_{[100]}$, $Al_2O_{3[100]}$ and $CaO_{[100]}$ (subscript $_{[100]}$ means 100% volatile-free silicate basis) and Mg/Al ratios (data from Song et al. 2009). The olivine-sulfide cumulate has high $MgO_{[100]}$ and low $Al_2O_{3[100]}$ and $CaO_{[100]}$ (Fig. 2a1-a3). In drill-hole ZK48-2 intersecting the No. 2 orebody, $MgO_{[100]}$ and Mg/Al ratios increase gradually upward from the sulfide-bearing olivine pyroxenite to the sulfide-lherzolite, whereas $Al_2O_{3[100]}$ and $CaO_{[100]}$ decrease (Fig. 2c1-c4). Plots of binary diagrams of Si/Ti vs. (Mg + Fe)/Ti and [4Ca + 4Na + 0.5(Mg + Fe)]/Ti vs. (Si + Al)/Ti molar ratios on 100% silicate basis indicate that olivine is the main cumulus phase in the sulfide-olivine cumulate and lherzolite from different locations of No. 2 orebody (ESM Fig. 4) (Pearce 1968; Stanley and Russell 1989).

Chalcophile element compositions

As shown in Fig. 3, although the various types of ores from the No. 2 and No. 2a orebodies have similar Ni grades to their counterparts in the No. 1, No. 24 and No. 3 orebodies, they have lower PGE grades. Cu-rich ores have not been reported in the No. 2 orebody. The Cu-rich ores from No. 1 and 24 orebodies have anomalously high Cu grades

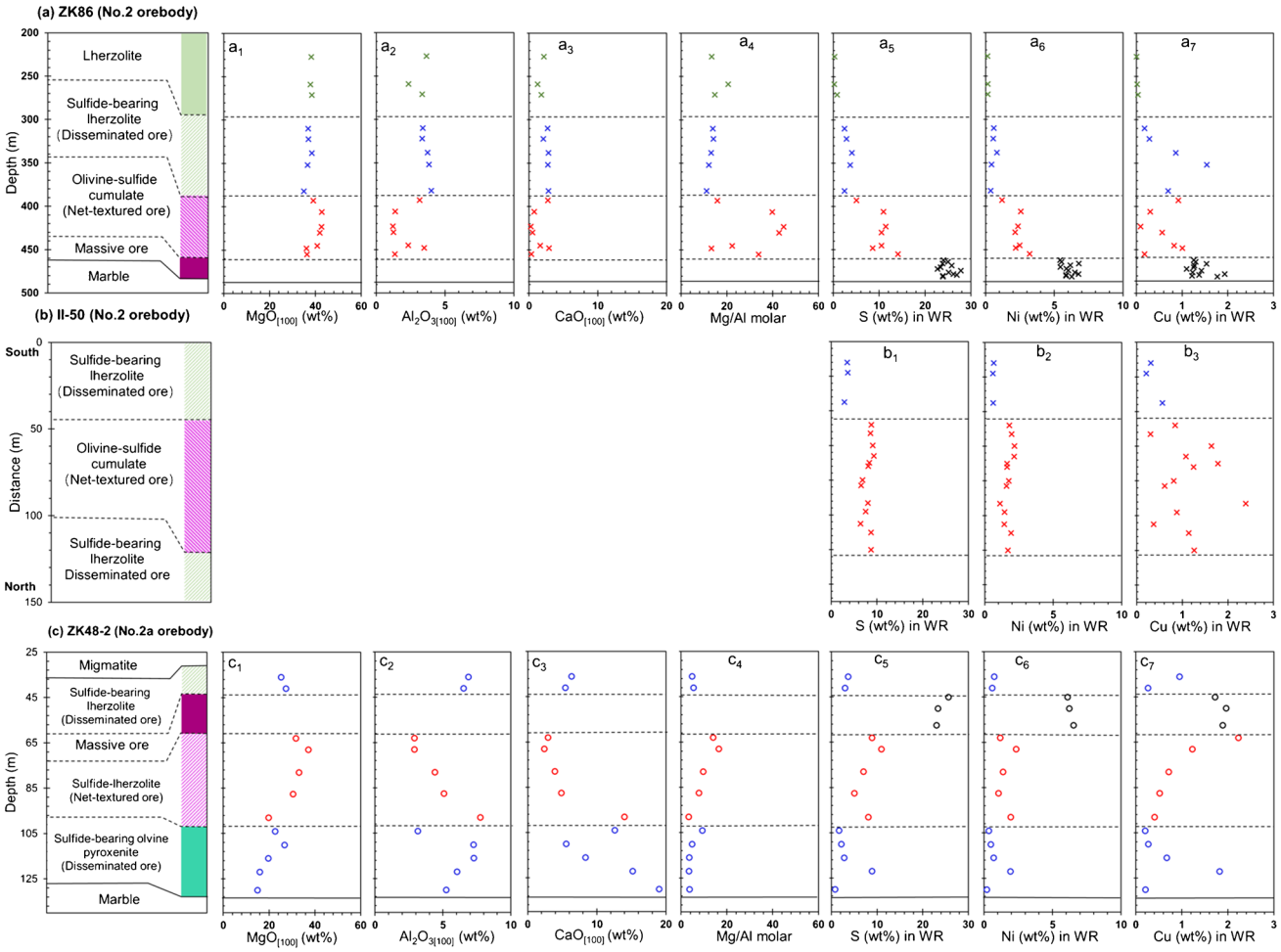

Fig. 2 Stratigraphic variations of recalculated major oxides of whole-rocks in 100% silicate basis ($MgO_{[100]}$, $Al_2O_{3[100]}$, $CaO_{[100]}$) and atomic ratio of Mg/Al, whole-rock contents of S, Ni and Cu of drill-hole ZK86 (a_1-a_7), underground tunnel at elevation 1150 m of exploration line II-50 (b_1-b_3) and drill-hole ZK48-2 (c_1-c_7) cutting through the No. 2 and No. 2a orebody (the newly discovered extension) orebodies. Sulfide ores from II-50 were only measured S, Ni, Cu and PGE. Data of drill-hole ZK86 are from Song et al. (2009), WR = whole rock

(1.1–6.25%), relatively high Pt, Pd grades and low Ir grades (Fig. 3) (Chai and Naldrett 1992; Chen et al. 2013).

Contents of PGE, Ni and Cu of the sulfide ores are recalculated to 100% sulfide (Barnes and Lightfoot 2005). Olivine in the net-textured and disseminated sulfides contains 1520—2490 ppm Ni (2060 ppm in average), which is slightly higher than Ni contents of olivine in barren rocks (Ni = 1677—2211 ppm, 1830 ppm in average) (Li et al. 2004). 30–70% olivine in the sample could cause a deviation of Ni about 69 to 151 ppm, which is negligible for disseminated and net-textured sulfide ores which contain ~ 5000 and 20,000 ppm Ni on average. Nickel in olivine is subtracted from whole rock Ni content before calculating the Ni contents of sulfides using the correlation between MgO and Ni in sulfide-free lherzolites and sulfide-olivine cumulates at Jinchuan (De Waal et al. 2004; Song et al. 2006, 2009). Figure 4 shows that the various types of ores from the No. 2a and No. 2 orebodies contain similar $Ir_{[100]}$, $Ru_{[100]}$, $Rh_{[100]}$, $Pt_{[100]}$ and $Pd_{[100]}$ (subscript$_{[100]}$ means the content in 100% sulfide) but lower PGE contents than similar ores from other orebodies. In the binary diagrams, $Ru_{[100]}$ and $Rh_{[100]}$ are positively correlated to $Ir_{[100]}$, whereas $Pd_{[100]}$ and $Pt_{[100]}$ are weakly correlated to $Ir_{[100]}$ (Fig. 5a-d). The sulfide ores from the No. 2 orebody show distinctly lower $Pd_{[100]}$ than those from other orebodies and a larger variation in $Pt_{[100]}$ (Fig. 5e).

In chemostratigraphic columns of the drill-hole ZK86 (Fig. 6a1-a6), $IPGE_{[100]}$ of the basal massive ore decreases upward, whereas $Pt_{[100]}$, $Pd_{[100]}$ and Pd/Ir tend to increase. In contrast, $PGE_{[100]}$ rises distinctly upward and Pd/Ir ratio decreases in the net-textured ore, whereas the overlying disseminated ores display opposite trends (Fig. 6a1-a6). In the underground tunnel along exploration line II-50, which

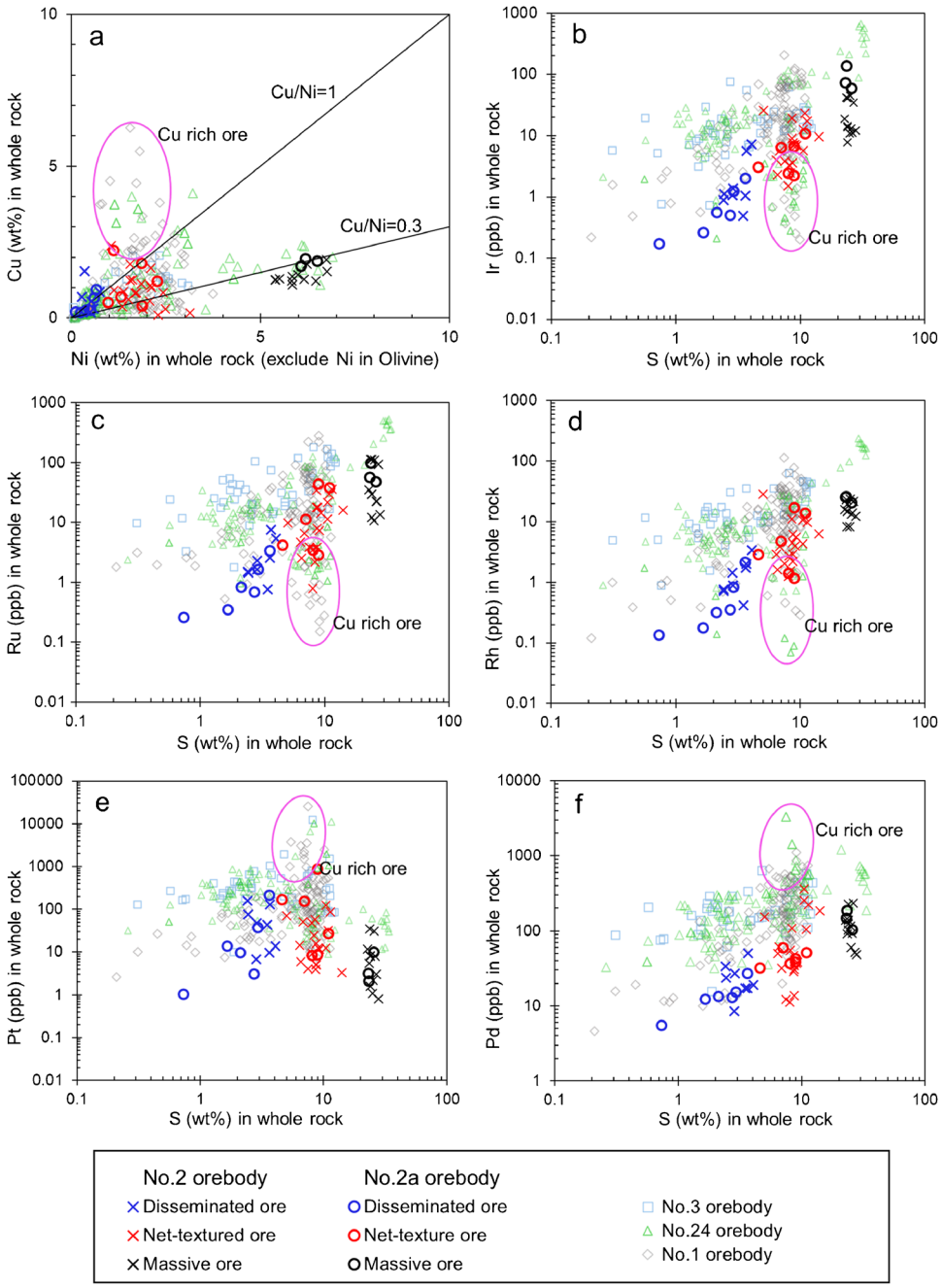

Fig. 3 Binary diagrams of (**a**) Ni against Cu and (**b-f**) S against PGE of the sulfide ores from the four large orebodies of the Jinchuan deposit. Ni in olivine of the sulfide ores has been subtracted from whole-rock compositions using the method proposed by De Waal et al. (2004). Data of No. 1, No. 3 and No. 24 orebodies are from Chai and Naldrett (1992), Su et al. (2008), Song et al. (2009), Tonnelier (2010), Chen et al. (2013), Duan et al. (2016) and Kang et al. (2022)

is located near the drill-hole ZK48-2 (Fig. 1d), $IPGE_{[100]}$ values of the net-textured ore also rise upward along with decreasing Pd/Ir value, except for the samples from the lower part (Fig. 6b1-b3, b6). Chemostratigraphic columns of the drill-hole ZK48-2 (Fig. 6c1-c6) show that vertical variations of $PGE_{[100]}$ of the net-textured and disseminated ores as well as massive ores of the No. 2a orebody (ZK48-2) are similar to the same ore types in the drill-hole ZK86, although the sequences of the ore types are different (ESM Fig. 2).

Discussion

Relationship between No. 2 and No. 2a orebodies

As mentioned above, many bore holes drilled completed between No. 1 and No. 2 orebodies in exploration programs have revealed no connection between the two orebodies. Thus, the orientation of magma flow of No. 2 orebody should not be East–west. The size and boundaries of the No. 2 orebody have already been delineated during the exploration programs (Fig. 1d), whereas the ends of the No. 2a

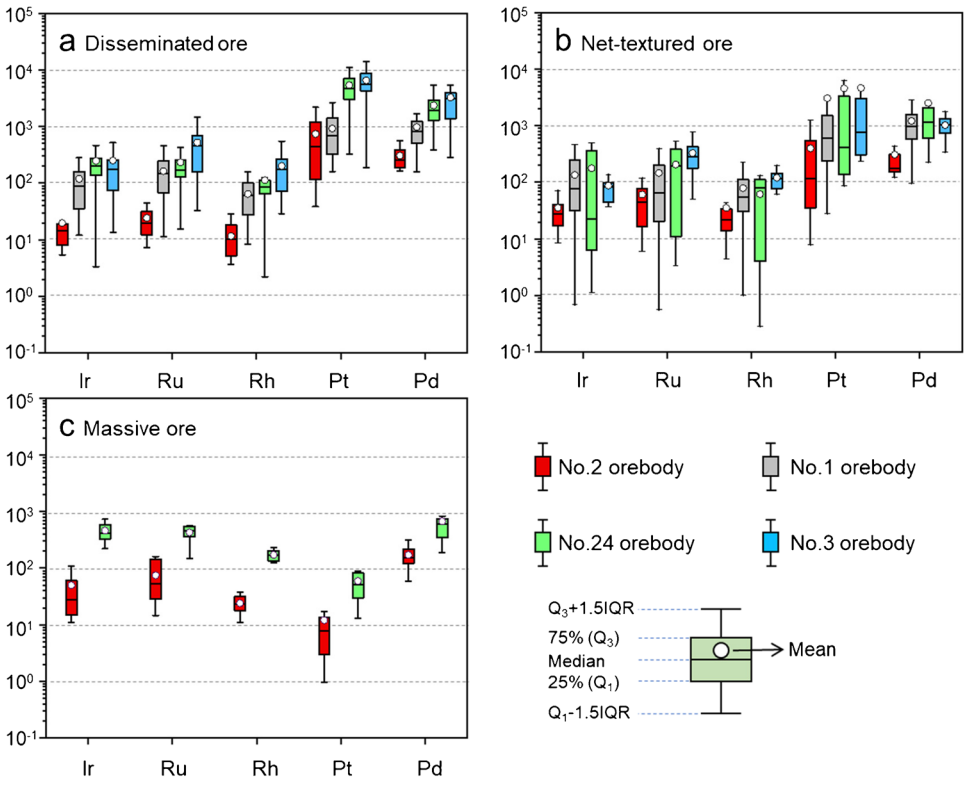

Fig. 4 Comparison of PGE tenors for (**a**) disseminated, (**b**) net-textured and (**c**) massive ore between the four largest orebodies in Jinchuan deposit. The central box is the middle 50% of the data set from the lower quartile (Q_1, which represents the 25th percentile) to the uppper quartile (Q_3, which represent the 75th percentile); Central line and blank cicle in the box denote the median and mean, respectively. The lower and upper whisker represent the range of 1.5*(Q_3-Q_1) from the box. Data of the orebodies No. 1, 24 and 3 and part of No. 2 orebodies are from Chai and Naldrett (1992), Su et al. (2008), Song et al. (2009), Tonnelier (2010), Chen et al. (2013), Duan et al. (2016) and Kang et al. (2022)

orebody have not been intersected by drill holes (Fig. 1e). A downward extension of No. 2a orebody is still a possibility potential. Because the Jinchuan intrusions were originally sub-horizontal (De Waal et al. 2004; Song et al. 2012), No. 2a should have been deposited upstream of No. 2 orebody in a sulfide-bearing magma conduit. Therefore, both No. 2a and No. 2 orebodies have similar Ni, Cu, PGE contents and chemostratigraphic variations of $PGE_{[100]}$ among the various ore types (Figs. 3, 5, 6).

Parental magma PGE compositions of No. 2 orebody

Previous studies on radioactive isotopes of the Jinchuan rocks and the composition of olivine suggested a metasomatised mantle source for the primary magma (Li et al. 2005; Tonnelier 2010; Lu et al. 2019). Thus, the PGE distributions of the parental magma probably reflect the metasomatised mantle source (Lesher and Stone 1996). The initial PGE compositions of immiscible sulfide liquids depend on PGE abundances in the parental magma and the mass ratio of silicate magma/sulfide liquid (R factor; Campbell and Naldrett 1979). The scattered distribution of sulfides in the disseminated ores inhibit macroscopic fractionation of PGE because the sulfide droplets are isolated (ESM Figs. 2b, g, 3a, d). Thus, PGE tenors of the disseminated ores should reflect the PGE compositions of the sulfide liquids initially segregated from silicate melts (e.g., Barnes and Maier 1999).

Because of the crustal sulfur has been incorporated by the Jinchuan magma (Ripley et al. 2005; Tonnlier 2010), the equation proposed by Lesher and Burnman (2001) is used to model sulfide segregation:

$$Y_f = \left(X_0 R + X_i\right) D/(R + D) \quad (1)$$

In the formulae, Y_f is the final content of metal in the sulfide melt, X_0 is the initial metal content in magma, X_i is the metal concentration of metal in the crustal sulfide that the magma incorporated (assuming ~ 0 in this paper), D is the partition coefficient of metal between sulfide and magma. If it is assumed that $D_{Ir}^{sul/sil}$ and $D_{Pd}^{sul/sil}$ are ~ 400,000 (Mungall and Brenan 2014), calculations using the Eq. (1) indicate that the parental magma contained ~ 0.01 to 0.05 ppb Ir and 0.2 to 0.8 ppb Pd. $D_{Ni}^{sul/sil}$ varies with f_{O2} and content of FeO of the magma (Li and Audétat 2012; Kiseeva and Wood 2013). Based on the FeO contents of the Jinchuan parental magma (10.3–14.4%, Tonnelier 2010) and f_{O2} proposed (+0.5 ~ +0.6, Duan et al. 2016; Mao et al. 2018), $D_{Ni}^{sul/sil}$ may vary from 200 to 700 (Li and Audétat 2012; Kiseeva and Wood 2013). This results in Ni contents of the parental magma from 240 to 500 ppm. This means that the parental magma of No. 2 orebody is slightly more PGE-depleted than those of the No. 1, No. 3 and No. 24 orebodies (Song et al. 2009; Chen et al. 2013; Kang et al. 2022). On the other hand, Tonnelier (2010) argued that the No. 2 orebody has high relatively f_{O2} (up to FMQ + 2.7) compared to the other

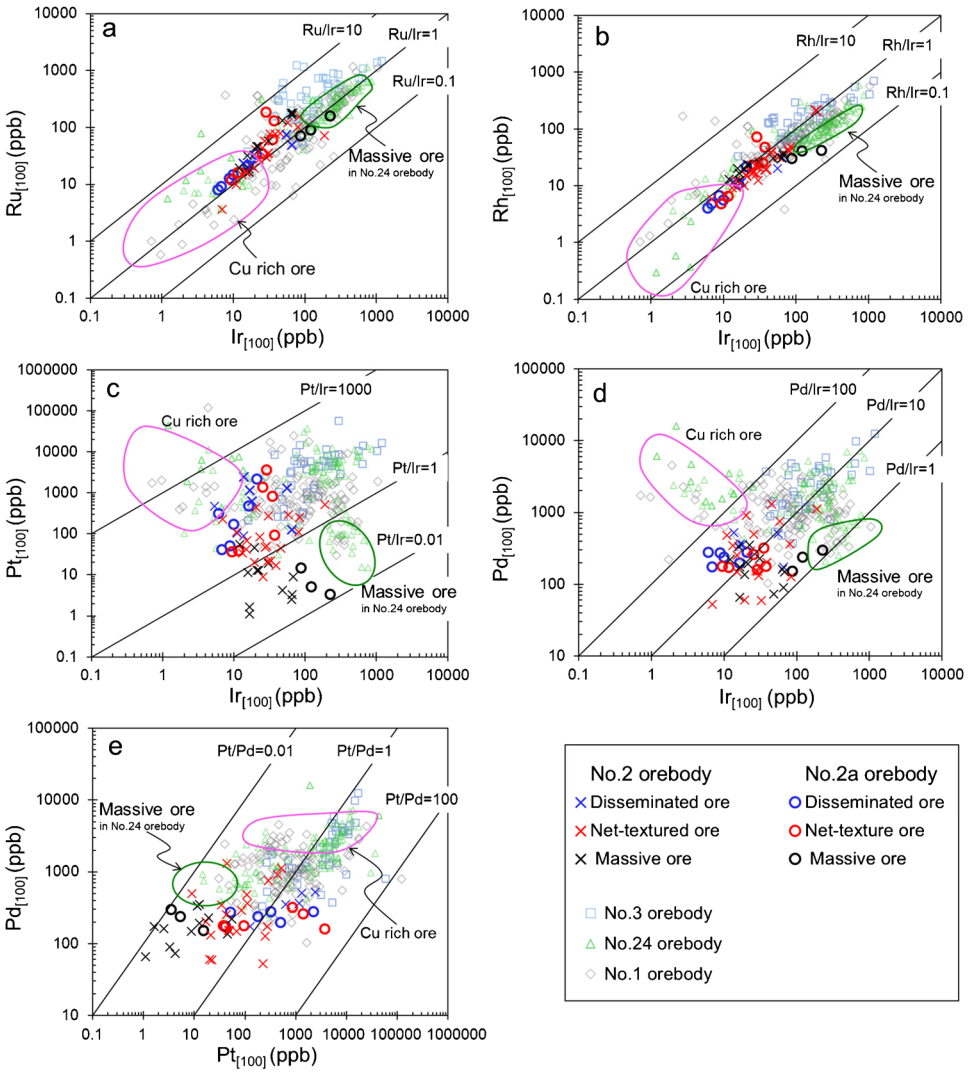

Fig. 5 Comparisons of PGE tenors of the sulfide ores from four large orebodies of the Jinchuan deposit. The PGE data of No.1, No. 3 and No. 24 orebodies are from Chai and Naldrett (1992), Su et al. (2008), Song et al. (2009), Tonnelier (2010), Chen et al. (2013), Duan et al. (2016) and Kang et al. (2022)

orebodies at Jinchuan. High f_{O2} may result in decrease of $D_{Ni}^{Sul/Sil}$ (Li and Audétat 2012) which has a small effect on the partition coefficients of PGE between sulfide liquid and silicate melt (Bezmen et al. 1994). Thus, the relatively low PGE tenors of the No. 2 and No. 2a orebodies are associated with either PGE-depletion of the parental magma or relatively low R values. Correspondingly, the sulfide ores of the No. 2 orebody have lower PGE tenors but higher Cu/Pd ratios than those of other orebodies (Fig. 4, ESM Fig. 5).

IPGEs are more compatible in chromite than in olivine and pyroxene, Pd is incompatible with regard to mafic minerals, but Pt is moderately compatible in pyroxene and incompatible in olivine (ESM Table 4) (Capobianco et al. 1994; Puchtel and Humayun 2001; Ely and Neal 2002; Righter et al. 2004). Therefore, high contents of chromite in the sulfide ores may result in enrichments of IPGE. As described by Barnes and Tang (1999), the Jinchuan rocks and ores contain less than 1.0 vol% chromite, which is commonly enclosed in olivine. Additionally, because olivine-sulfide dihedral angles of net-texture ores in No. 2 orebody range from 52° to 55° and are less than the 60° limit above which no wetting takes place (Tonnelier 2010), the sulfides in the ores could wet olivine (ESM Fig. 2). The positive correlations among S, Cr and MgO/Al_2O_3 indicate that the net-textured ores commonly have higher contents of olivine and chromite than the disseminated sulfides (ESM Fig. 6). The relative high IPGE contents in the net-textured ores compared to the disseminated sulfides at a given Cr content indicate that PGE are dominantly contained in sulfides rather than in chromite (ESM Fig. 7).

Fractionation of chromite, olivine and pyroxene would lead to decreasing IPGE contents and increasing Pd/Ir ratio in the basaltic magma. Sulfide removal could result in depletion of PGE without variation of Pd/Ir ratio of the parental magma. Thus, low PGE tenors and varying Pd/Ir values of the disseminated ores of the No. 2 orebody indicate that the different batches of magma experienced variable degrees of fractional crystallization of mafic minerals and sulfide

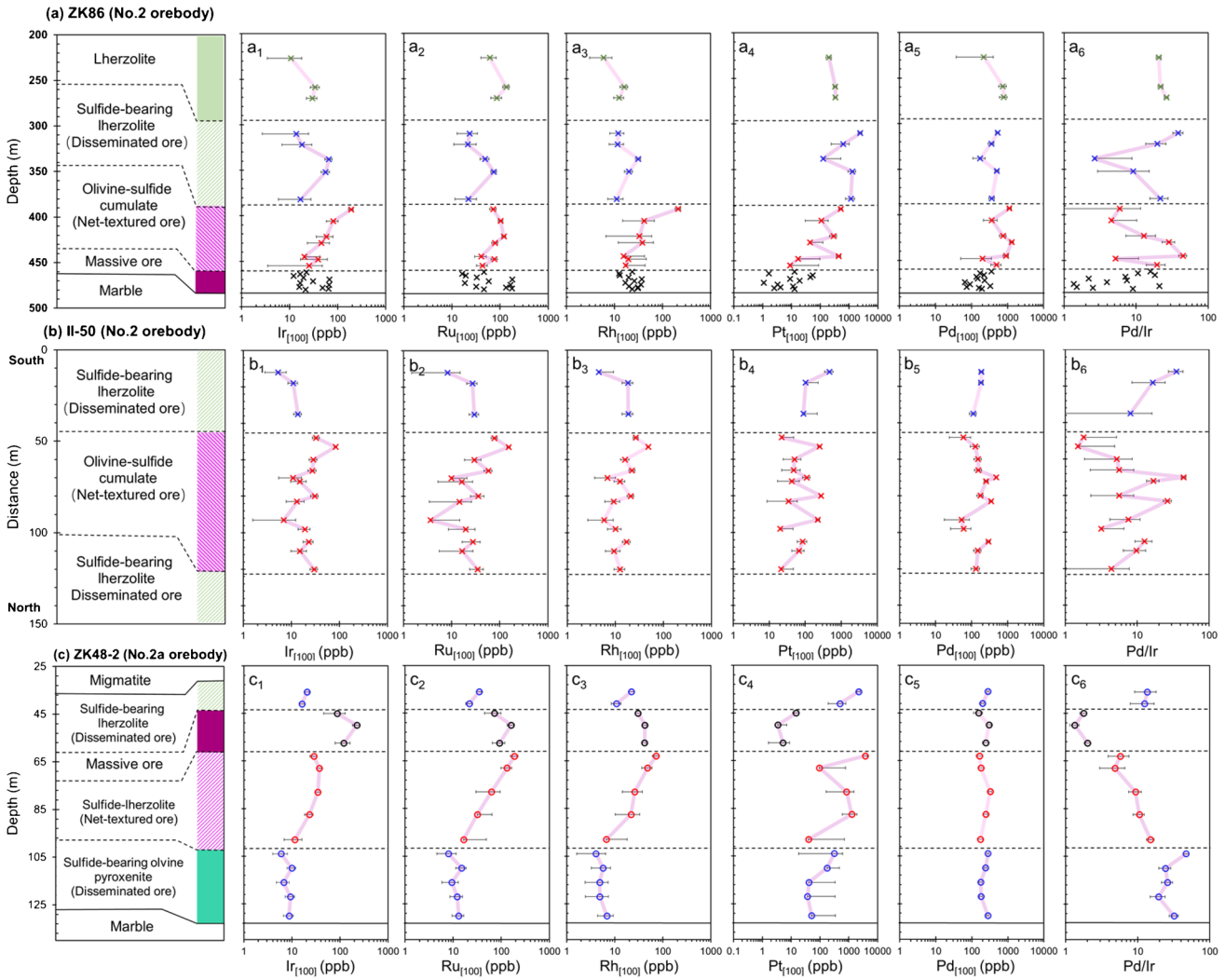

Fig. 6 Stratigraphic variations of PGE tenors, Pd/Ir and Cu/Ni ratio for the drill-holes ZK86 (a_1-a_6), underground tunnel at elevation 1150 m of exploration line II-50 (b_1-b_6) and ZK48-2 (c_1-c_6) cutting through the No. 2 and No. 2a (the newly discovered extension) orebodies. The error bar is standard error. Data of the drill-hole ZK86 are from Song et al. (2009)

removal at a range of R values prior to final emplacement (Fig. 7).

Timing and location of sulfide saturation

Sulfur solubility of basaltic magma increases with decreasing pressure (Mavrogenes and O 'Neill 1999). Sulfide saturation in the ascending magma is difficult to be reached without addition of external sulfur by contamination with S-bearing crustal material (Lesher and Burnham 2001; Ripley and Li 2003; Keays and Lightfoot 2010; Lesher 2017). Non-zero $\delta^{34}S$ values of the Jinchuan sulfide ores and the barren wall rocks suggest that the crustal contamination occurred before the magmas entered the Jinchuan intrusion (Ripley et al. 2005). On the other hand, elevation of f_{O2} could convert Fe^{2+} into Fe^{3+} and reduce S solubility of the magma (Li and Ripley 2005). Lehmann et al. (2007) proposed that decomposition of contact marble could release CO_2 into magma, leading elevation of f_{O2} and reduction of sulfur content of the magma at sulfide saturation. Thus, both external sulfide addition via contamination at depth and decomposition of contact marble may contribute to sulfide segregation at Jinchuan (Tonnelier 2010). In view of the high density of the sulfide liquid relative to the basaltic magma, sulfides were more likely transported horizontally for significant distances relative to be transported upward (Lesher 2019). An alternative possible mechanism of addition of external sulfide leading to S-saturation in the magma is that sulfides in the metamorphic rocks of Baijiazuizi Formation were melted when the magma passed through the strata horizontally (Lesher 2017, 2019).

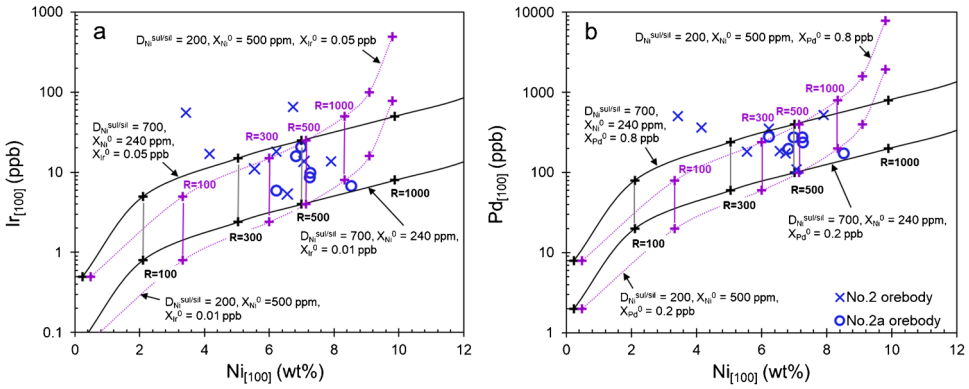

Fig. 7 Plots of the disseminated ores from No. 2 orebody in (**a**) Ni vs Ir and (**b**) Ni vs Pd on a 100% sulfide basis. Model curves in the plots shows the content variation of sulfides equilibrium with magma contain 0.01 to 0.05 ppb Ir and 0.2 to 0.8 ppb Pd and 240 to 500 ppm Ni at various R factor (Campbell and Naldrett 1979). Partition coefficients of Ir and Pd ($D_{Ir,Pd}^{sul/sil}$ ~ 400,000, Mungall and Brenan 2014) and Ni ($D_{Ni}^{sul/sil}$ range from 200 to 700, Li and Audétat 2012; Kiseeva and Wood 2013) were used in the calculation. The concentration of Ni in olivine have been excluded based on equation: Log Ni(ppm) = 0.016MgO(%) + 2.475 according to De Waal et al. (2004), before recalculated it to 100% sulfide. Data from the No. 2 orebody are from Song et al. (2009)

Fractionation of sulfide melts

Fractionation of MSS can lead to fractionation of IPGE and PPGE in the sulfide ores because Os, Ir, Ru, and Rh are compatible in MSS, whereas Pt, Pd, Au, and Cu are incompatible (Li et al. 1996; Barnes et al. 1997) (ESM Table 4). Because the different types of ores display highly variable $Pt_{[100]}$ (see below), the Pd/Ir ratio is used as indicator of fractionation of IPGE and PPGE.

Positive correlations of atomic ratios between Si/Ti and (Mg + Fe)/Ti and between (4Ca + 4Na + 0.5(Mg + Fe))/Ti and (Si + Al)/Ti demonstrates that olivine is the dominant cumulate mineral in the sulfide-olivine cumulate and lherzolite (ESM Fig. 4) (Pearce 1968; Stanley and Russell 1989) (Lesher 2019). Li et al. (2004) suggested that the olivine in the sulfide-olivine cumulate of the No. 2 orebody crystallized dominantly at depth based on a small range in forsterite content (Fo) (82% to 86%). However, Tonnelier (2010) argued that at least 25–30% olivine crystallized in-situ. An increase in $MgO_{[100]}$ and Mg/Al of the sulfide-lherzolite (net-textured ore) in ZK48-2 indicates that the amount of the olivine deposited from different batches of magmas increases upward (Fig. 2c1, c4). A Slight upward increase of forsterite content (Fo) of olivine in the net-textured olivine-sulfide cumulate in the No. 2 orebody indicates that the magmas experienced progressively less differentiation prior to crystallization of the olivine (Li et al. 2004). Upward increases of PGE tenors and decreases of Pd/Ir ratios of the net-textured ores in both the No. 2 and No. 2a orebodies cannot be explained by in-situ fractionation of the sulfide liquid (Fig. 6). The increases indicate that the sulfides segregated under progressively higher R values and/or reaction between the sulfide liquid and less evolved magmas.

Noteworthy decreases of $IPGE_{[100]}$ and increases of Pd/Ir in the disseminated ores from the drill-hole ZK86 and underground tunnel II-50 through No. 2 orebody can be attributed to sulfide segregation from the magmas under progressively smaller R values by sulfide deposition in slow-flowing magma (Figs. 6a1-a3, a6, b1-b3, b6) (Lesher 2019). This is because macroscopic differentiation is very difficult among the isolated sulfide clusters in the disseminated ores (ESM Figs. 2b, 3a) (Mungall 2002; Barnes et al. 2013). In contrast, small variations of $IPGE_{[100]}$ and Pd/Ir in the basal disseminated ores of No. 2a orebody (ZK48-2) indicate that the sulfide liquids segregated under similar R values (Fig. 6c1-c3, c6).

Close-spaced sampling of the massive ore lens in drill-hole ZK86 shows decreasing $IPGE_{[100]}$ and increasing $Pt_{[100]}$, $Pd_{[100]}$ and Pd/Ir upward (Fig. 6a1-a6) (Song et al. 2009). Although only three massive ore samples in drill hole ZK48-2 were analyzed, $PGE_{[100]}$ and Pd/Ir ratio show similar upward trends (Fig. 6c1-c6). These variations suggest *in-situ* fractionation of sulfide liquid in the massive ores independent of the adjacent net-textured ore in the No. 2 and No. 2a orebodies. The sharp contacts between the massive ore and net-textured ore (Fig. 1d-e, ESM Fig. 1) and xenoliths of net-textured or disseminated ores and lherzolite in the massive ores suggest that the massive ores were the result of emplacement of pure sulfide melt. The pure sulfide melt was possibly filter pressed squeezed from somewhere else, or it might have segregated from the net-textured sulfides (Tonnelier 2010). Similar relationships have been observed at the Eagle Ni-Cu-(PGE) deposit (Michigan, USA), in which massive ore shows sharp boundaries and has PGE tenors distinct from the net-textured ore above and below, suggesting later emplacement of pure sulfide melt (Ding et al. 2012).

Alternative interpretation for Pt depletion in massive ore

The massive ores in the No. 2 orebody have lower Pt contents (1—55 ppb) and Pt/Pd ratios (0.01—0.33) than the above net-textured ores ($Pt_{[100]}$ = 440 ppb and Pt/Pd = 2.2 in average) (Fig. 6a4 and a6). The massive ores in the No. 2a orebody contain 3—15 ppb Pt, which is much less than $Pt_{[100]}$ (1017 ppb in average) of the underling net-textured ores (Fig. 6c4 and c6). Additionally, all the massive ores display extensive Pt-depletion relative to Rh and Pd (ESM Fig. 8c). Massive ores characterized by Pt depletion are not unusual and have been reported in some other Ni-Cu sulfide deposits, such as Selkirk and Phoenix in Eastern Botswana, Mount Keith and Nova-Bollinger in Australia (Maier et al. 2008; Barnes et al. 2012, 2022). Song et al. (2009) have suggested two possible mechanisms causing the Pt depletion in the massive ore of No. 2 orebody: (1) Pt-Fe alloy fractionation from basaltic magma before sulfide segregation (ESM Table 4) (Fleet et al. 1993; Li et al. 1996). However, if Pt-Fe alloy was removed from the basaltic magma before sulfide segregation, the net-textured and disseminated ores should also show Pt depletion, which is not the case (ESM Fig. 9a, b). (2) metamorphic-hydrothermal alteration of the massive ores.

It is generally considered that Pd and Pt have similar geochemical behaviors during sulfide segregation and fractional crystallization (e.g., Li et al. 1996; Barnes et al. 1997 and references therein). The solubilities of both Pt and Pd in hydrothermal fluids are positively correlated with f_{O2}, temperature, acidity and chlorinity (e.g., Sullivan et al. 2022a, b), thus, they could be mobile in the fluids (Hanley et al. 2005; Le Vaillant et al. 2015; Holwell et al. 2017). However, thermodynamic modelling based on published experimental data suggested that Pd is more soluble than Pt in hydrothermal fluids in sulfide rich environments (Barnes and Liu 2012). A remarkable feature of the massive ores from the No. 2 and No. 2a orebodies is the Pt-depletion and decoupling between Pt and Pd (ESM Fig. 8c). In contrast, the net-textured and disseminated sulfides, which have been extensively altered, show either Pt-depletion or Pt-enrichment (ESM Figs. 3a-d, 8a, b). The net-textured ores rather than the massive ores contain secondary magnetite, indicating that the former experienced more extensive hydrothermal alteration accompanied by serpentinization of olivine (ESM Figs. 3a-d). During the alteration, pyrrhotite in the net-textured ores was decomposed to magnetite and pyrite (possible reaction: $3Fe_9S_8 + 10O_2 = 5Fe_3O_4 + 12FeS_2$). However, the occurrence of magnetite at the margins of sulfides and the rarity of pyrite in the net-textured ores (ESM Figs. 3b and e) suggests that the pyrite might have been decomposed and disappeared because sulfur was lost rather than addition of S during the hydrothermal alteration. Additionally, agreement of Re-Os ages of the massive ores (867 ± 75 Ma) (Yang et al. 2008) with zircon SHRIMP U–Pb ages (827 ± 8 Ma) for the Jinchuan intrusion (Li et al. 2004) points to only weak hydrothermal alteration in the massive ores (ESM Fig. 3c, f). In contrast, Re-Os ages of the disseminated ores yielded an age of 1117 ± 67 Ma due to hydrothermal alteration (Yang et al. 2008). Therefore, the Pt-depletion of the massive ores is difficult to be attributed to hydrothermal alteration.

Alternatively, the Pt depletion of the massive ores could be due to nugget effect caused by existence of heterogeneously distributed Pt-rich minerals (e.g., Savard et al. 2010). However, the nugget effect would become negligible when the sizes of Pt-rich minerals are less than 50 μm because in that case the Pt-rich grains are relative homogeneously distributed (Barnes et al. 2022). Recent study revealed that $Pt_{[100]}$ is positively correlated with $As_{[100]}$ in the Jinchuan sulfide ores and that base-metal minerals have low Pt contents (Chen et al. 2015). Thus, Pt was speculated to be hosted predominantly by sperrylite grains, which commonly measure less than 10 μm in the Jinchuan sulfide ores (Prichard et al. 2013; Dong et al. 2021). However, sperrylite crystals have not been observed in the massive ores under microscope and scanning electron microscope. As shown in Fig. 8b-e, 15 out of 16 parts divided from the 4 massive ore hand specimens consistently display Pt depletion. Thus, Pt depletion of the massive ores most likely does not result from nugget effects. Additionally, the massive ores from drillhole ZK86 display comparable Pt depletions (ESM Fig. 8c) (Song et al. 2009). Recent experiments revealed that pentlandite can be formed via peritectic reaction between MSS and fractionated sulfide liquid at 870—800 °C (Waldner and Pelton 2004; Kosyakov and Sinyakova 2012; Kitakaze et al. 2016). These studies indicated that not all pentlandite forms via sub-solidus exsolution from MSS. Both Pt and Pd are incompatible to MSS and ISS and tend to concentrate in residual sulfide liquids (Li et al. 1996; Mungall et al. 2005; Liu and Brenan 2015). In situ LA-ICPMS measurements have indicated that pentlandite from many magmatic sulfide deposits is remarkably enriched in Pd relative to pyrrhotite and chalcopyrite (Barnes et al. 2008; Dare et al. 2010; Chen et al. 2015; Liang et al. 2019; Mansur et al. 2021). This prompted Mansur et al (2019, 2021) to propose that Pd enters into the granular and contact pentlandite between pyrrhotite and chalcopyrite from the fractionated sulfide liquid during the peritectic reaction. Pt remains in the sulfide liquid and is thus decoupled from Pd. The sulfide cumulates would become Pt depleted when the residual sulfide liquid migrated away. This model is consistent with the Pt depletion of the massive ores (ESM Fig. 8c), the high Pd contents of the pentlandite (up to 21 ppm) (Chen et al. 2015), and the relatively high $Pt_{[100]}$ (up to 3700 ppb) of a few net-textured or disseminated ores above or underneath the massive ores (Fig. 6a4, c4).

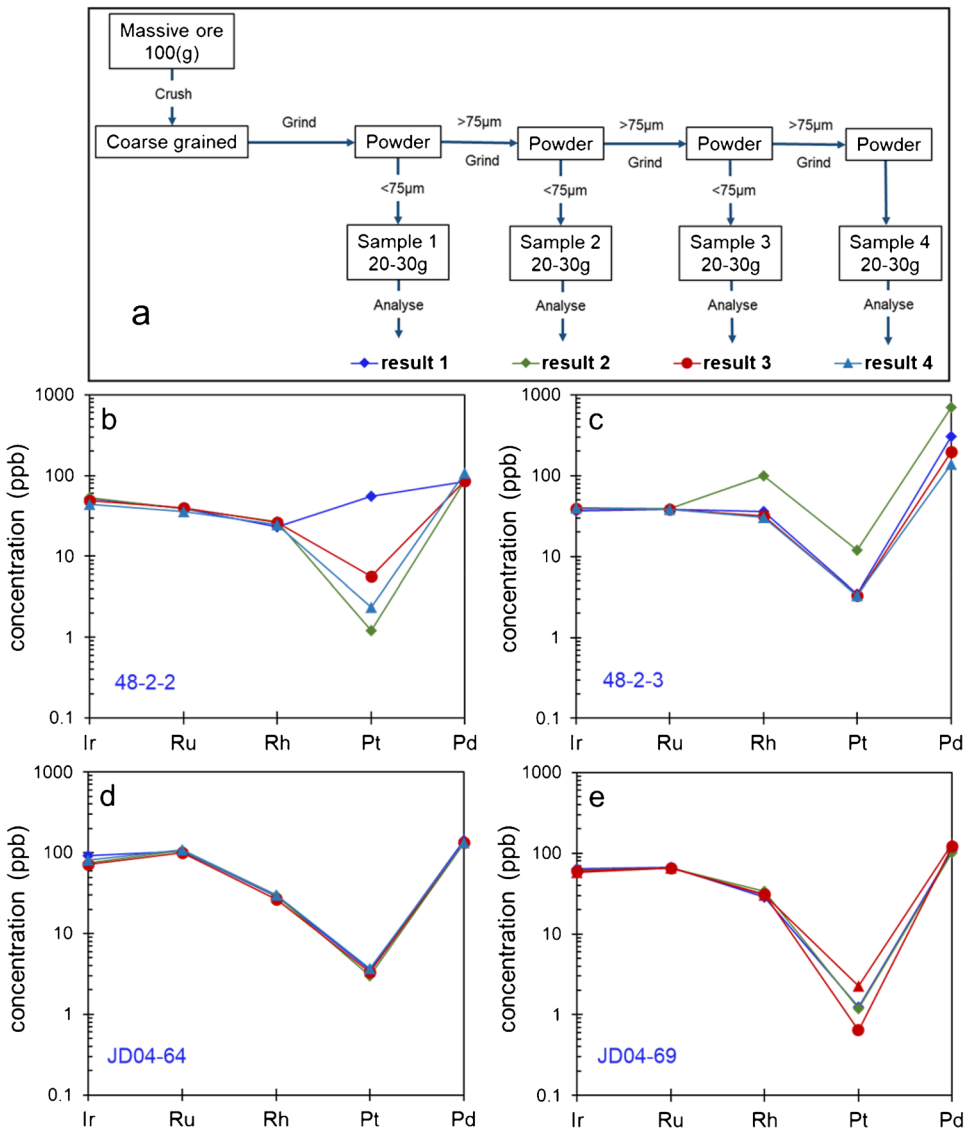

Fig. 8 (**a**) Schematic diagram and (**b**-**e**) comparison of PGE concentrations four divided parts of each massive ore. Every part divided from the same sample has similar PGE compositions and consistent depletion of Pt, except for only one part of the sample 48–2-2

Model for the formation of the No. 2 orebody

Previous studies indicated that the Jinchuan intrusion was originally subhorizontal. It was segmented and was rotated to its present subvertical orientation during late nappe tectonic movement of the Longshou terrane (De Waal et al. 2004; Song et al. 2012). Geological and geochemical features indicate that the No. 2a and No. 2 orebodies represent the upstream and downstream environments of the magma flow, respectively (Figs. 1, 2, 6). There are four mineralization stages:

Stage I (Fig. 9a): Basaltic magma reached various degrees of S-saturation due to crustal contamination with sulfidic material on the pathway of the magma. When the magma flow slowed down at wider segments of the magma conduit, the sulfide droplets settled down and olivine and pyroxene crystallized from the basaltic magma to form the sulfide-bearing olivine pyroxenite (disseminated sulfide) at the base of No. 2a orebody. Decomposition of contact marble could lead to elevation of f_{O2} and further sulfide segregation (Lehmann et al. 2007; Tonnelier 2010). The fine-grained texture of the olivine pyroxenite demonstrates that the magma cooled fast, accompanied by accumulation of small amount of olivine (Latypov 2015). Thus, the sulfide-bearing olivine pyroxenite has low values of $MgO_{[100]}$, Mg/Al and $IPGE_{[100]}$ and high Pd/Ir ratios relative to the overlying net-textured ores (Figs. 2c1, c4, 6c1-c3, c6).

Stage II (Fig. 9b): Following the first stage, more batches of basaltic magma pass through the magma conduit. Sulfides and olivine carried by the magma settled down to form the net-textured ores in lherzolite of No. 2a orebody. Increases

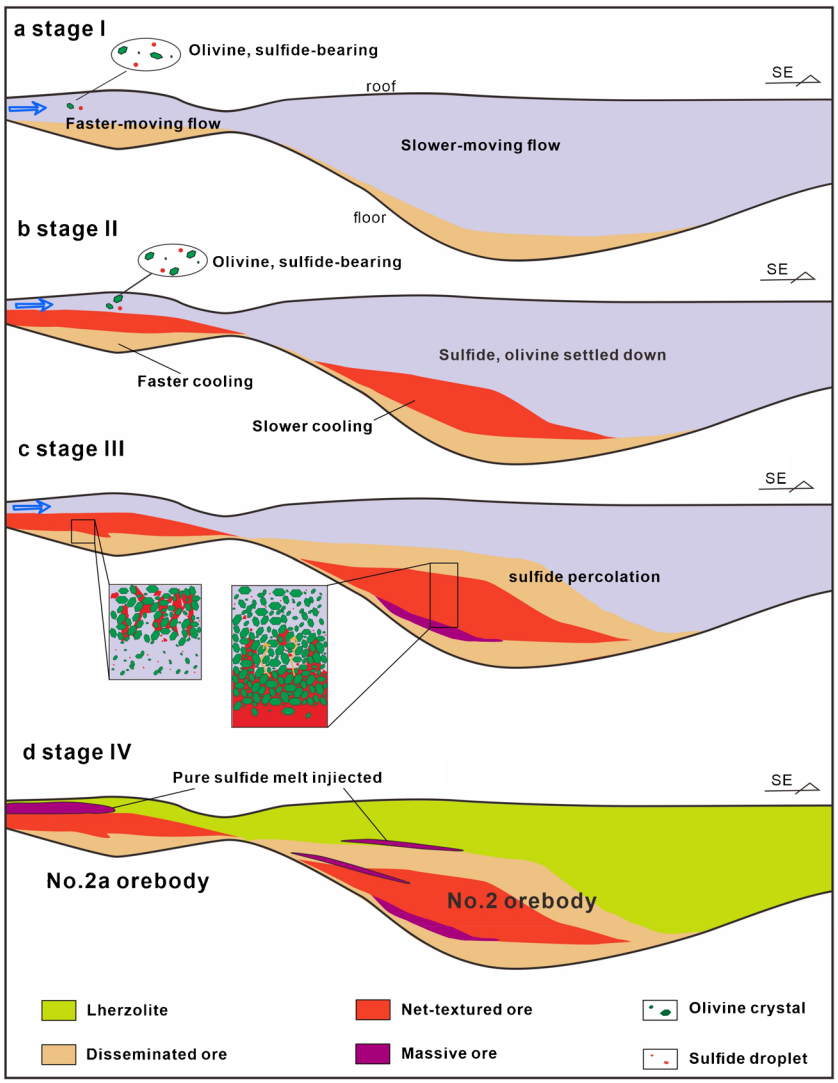

Fig. 9 Model of the formation of No. 2 orebody. Stage I: Sulfide-saturation magma reached the widen part of conduit, sulfide and olivine settled down from silicate melt. Stage II: More sulfide and olivine progressively settled down from silicate melt, the thinner No. 2a part cooling faster than the No. 2 part result in less olivine accumulated in No. 2a part. Stage III: Sulfide also downward percolation and form thicken net-textured ore in No. 2 orebody. Stage IV: Pure sulfide melt injected into No. 2a and No. 2 orebodies to form the massive ores that occur at the top the orebody

of $MgO_{[100]}$ and Mg/Al ratios as well as S contents upward in the lherzolite (Figs. 2c1, c4, c5) suggest that the amount of the olivine settling down from the batches of magma increases progressively. Deposition of more olivine led to thick sulfide-olivine cumulates having relatively high $MgO_{[100]}$ and Mg/Al (Figs. 2a1, a4). The sulfide liquids carried by different batches of magma segregated under progressively increasing R values. Thus, the net-textured ores of the No. 2 and No. 2a orebodies show an increase of $IPGE_{[100]}$ and decrease of Pd/Ir upward (Figs. 6a1-a3, c1-c3). Low olivine-sulfide dihedral angles of the net-texture ores in the No. 2 orebody (< 60°, Tonnelier 2010) suggest that the sulfides settled while adhering to olivine or percolated downward in the olivine cumulates. A similar mechanism was proposed for the formation of the net-textured ore in the No. 3 orebody at Jinchuan (Kang et al. 2022).

Stage III (Fig. 9c): From the following batches of basaltic magma, sulfides segregated under progressively smaller R values and accumulated together with waning magma flow and thus decreasing olivine capacity of the magma to carry crystals and sulfide. Thus, the formation of the disseminated sulfides overlying the net-textured ores in the No. 2 orebody might be associated with a slowdown of the magma entering a larger magma chamber (Figs. 1d-e, 9c). Hence, $IPGE_{[100]}$ tend to decrease and Pd/Ir increase upwards in the disseminated sulfides (Fig. 6a1-a3, a6, b1-b3, b6).

Stage IV (Fig. 9d): Pure sulfide melt from somewhere else injected into different portions of the No. 2 and No. 2a orebodies and formed the lenticular or irregular shaped massive orebodies (Fig. 1d, e). *In-situ* fractionation of the pooled sulfide melts resulted in upward decrease in IPGE contents and Pd/Ir increase in the massive ores (Fig. 6). Migration of the Pt and Cu enriched residual sulfide liquids not only resulted in Pt depletion in the massive ores but also Pt and Cu enrichment in some of the adjacent net-textured ores.

Conclusions

Different types of ore in the newly discovered No. 2a and No. 2 orebodies of the Jinchuan deposit have similar Ni, Cu and PGE compositions. No. 2a and No. 2 orebodies are located in the upstream and downstream segments, respectively, of a sub horizontal magma conduit. Sulfide segregation under progressively higher silicate/sulfide liquid ratios in the replenished magma, and/or reaction of the sulfides with more silicate magmas resulted in upward increasing $IPGE_{[100]}$ and a decrease Pd/Ir of the net-textured ores in the orebodies. The massive ores experienced in-situ fractionation as indicated by decreases of $IPGE_{[100]}$ and increase of Pd/Ir upwards. Pt-depletion in the massive ores and Pt-enrichment in some of the adjacent net-textured ores are the results of migration of highly fractionated sulfide liquids.

Supplementary Information The online version contains supplementary material available at https://doi.org/10.1007/s00126-023-01184-w.

Acknowledgements This work was financially supported by the National Science Foundation of China projects (42121003, 41772067, and 41630316) to X.-Y. Song. We thank Chusi Li of Indiana University for useful discussion, plus editing the abstract and conclusions of the first draft. We are indebted to Mr. Ya-Lin Gao, Mei-Lin Xiao and Yuan-Zhi Meng of Jinchuan Company for their logistic support in sampling, and to Dr. Da-Peng Wang and Ms. Yi-Fan Yin for their assistance in PGE analysis. Constructive reviews from MC Lesher, David Evans and Wolfgang Maier are greatly appreciated.

Declarations

Conflict of interest The authors declare that they have no competing financial interest.

References

Barnes S-J, Lightfoot PC (2005) Formation of magmatic nickel-sulfide ore deposits and processes affecting their copper and platinum-group element contents. Econ Geol 100:179–213

Barnes SJ, Liu WH (2012) Pt and Pd mobility in hydrothermal fluids: Evidence from komatiites and from thermodynamic modelling. Ore Geol Rev 44:49–58

Barnes S-J, Maier WD (1999) The fractionation of Ni, Cu and the noble metals in silicate and sulphide liquids. Short Course Notes-Geol Assoc Canada 13:69–106

Barnes SJ, Tang ZL (1999) Chrome spinels from the Jinchuan Ni-Cu sulfide deposit, Gansu province, People's Republic of China. Econ Geol 94:343–356

Barnes S-J, Makovicky E, Makovicky M, RoseHansen J, Karup-Moller S (1997) Partition coefficients for Ni, Cu, Pd, Pt, Rh, and Ir between monosulfide solid solution and sulfide liquid and the formation of compositionally zoned Ni-Cu sulfide bodies by fractional crystallization of sulfide liquid. Can J Earth Sci 34:366–374

Barnes S-J, Prichard HM, Cox RA, Fisher PC, Godel B (2008) The location of the chalcophile and siderophile elements in platinum group element ore deposits (a textural, microbeam and whole rock geochemical study): implications for the formation of the deposits. Chem Geol 248:295–317

Barnes SJ, Fiorentini ML, Fardon MC (2012) Platinum group element and nickel sulphide ore tenors of the Mount Keith nickel deposit, Yilgarn Craton, Australia. Miner Deposita 47:129–150

Barnes SJ, Heggie GJ, Fiorentini ML (2013) Spatial variation in platinum group element concentrations in ore-bearing komatiite at the Long-Victor Deposit, Kambalda Dome, Western Australia: enlarging the footprint of nickel sulfide orebodies. Econ Geol 108:913–933

Barnes SJ, Stanley CR, Taranovic V (2022) Compositions and nicu-platinum group element tenors of Nova-Bollinger Ores with implications for the origin of pt anomalies in platinum group element-poor massive sulfides. Econ Geol 117:1687–1707. https://doi.org/10.5382/econgeo.4894

Bezmen NI, Asif M, Brügmann G, Romanenko I, Naldrett A (1994) Distribution of Pd, Rh, Ru, Jr, Os, and Au between sulfide and silicate metals. Geochim Cosmochim Acta 58:1251–1260

Campbell IH, Naldrett AJ (1979) Influence of silicate-sulfide ratios on the geochemistry of magmatic sulfides. Econ Geol 74:1503–1506

Capobianco CJ, Hervig RL, Drake MJ (1994) Experiments on crystal/liquid partitioning of Ru, Rh and Pd for magnetite and hematite solid solutions crystallized from silicate melt. Chem Geol 113:23–43

Chai G, Naldrett AJ (1992) Characteristics of Ni-Cu-Pge Mineralization and Genesis of the Jinchuan Deposit, Northwest China. Econ Geol Bull Soc Econ Geol 87:1475–1495

Chen LM, Song XY, Keays RR, Tian YL, Wang YS, Deng YF, Xiao JF (2013) Segregation and fractionation of magmatic Ni-Cu-PGE sulfides in the western Jinchuan intrusion, northwestern China: insights from platinum group element geochemistry. Econ Geol 108:1793–1811

Chen LM, Song XY, Danyushevsky LV, Wang YS, Tian YL, Xiao JF (2015) A laser ablation ICP-MS study of platinum-group and chalcophile elements in base metal sulfide minerals of the Jinchuan Ni-Cu sulfide deposit, NW China. Ore Geol Rev 65:955–967

Dare SAS, Barnes SJ, Prichard HM (2010) The distribution of platinum group elements (PGE) and other chalcophile elements among sulfides from the Creighton Ni-Cu-PGE sulfide deposit, Sudbury, Canada, and the origin of palladium in pentlandite. Miner Deposita 45:765–793. https://doi.org/10.1007/s00126-010-0295-6

Ding X, Ripley EM, Li CS (2012) PGE geochemistry of the Eagle Ni-Cu-(PGE) deposit, Upper Michigan: constraints on ore genesis in a dynamic magma conduit. Miner Deposita 47:89–104

Dong Y, Wei B and Wang CY. 2021. Major types and occurrences of platinum-group minerals in the Jinchuan Ni-Cu-(PGE) sulfide deposit: Insights for PGE enrichment during hydrothermal alteration. Acta Petrol Sin (in chinese) 10: 2875–2888

Duan J, Li CS, Qian ZZ, Jiao JG, Ripley EM, Feng YQ (2016) Multiple S isotopes, zircon Hf isotopes, whole-rock Sr-Nd isotopes, and spatial variations of PGE tenors in the Jinchuan Ni-Cu-PGE deposit, NW China. Miner Deposita 51:557–574. https://doi.org/10.1007/s00126-015-0626-8

Ely JC, Neal CR (2002) Method of data reduction and uncertainty estimation for platinum-group element data using inductively coupled plasma-mass spectrometry. Geostand Newsl 26:31–39

Fleet ME, Chryssoulis SL, Stone WE, Weisener CG (1993) Partitioning of platinum-group elements and Au in the Fe-Ni-Cu-S system: experiments on the fractional crystallization of sulfide melt. Contrib Miner Petrol 115:36–44

Hanley JJ, Pettke T, Mungall JE, Spooner ETC (2005) The solubility of platinum and gold in NaCl brines at 1.5 kbar, 600 to 800°C: A laser ablation ICP-MS pilot study of synthetic fluid inclusions. Geochim Cosmochim Acta 69:2593–2611. https://doi.org/10.1016/j.gca.2004.11.005

Holwell DA, Adeyemi Z, Ward LA, Smith DJ, Graham SD, McDonald L, Smith JW (2017) Low temperature alteration of magmatic

Ni-Cu-PGE sulfides as a source for hydrothermal Ni and PGE ores: a quantitative approach using automated mineralogy. Ore Geol Rev 91:718–740

Kang J, Song X-Y, Long T-M, Liang Q-L, Barnes SJ, Chen L-M, Li D-X, Ai Q-X, Gao Y-L (2022) Lithologic and geochemical constraints on the genesis of a newly discovered orebody in the Jinchuan intrusion, NW China. Econ Geol 117:1809–1825. https://doi.org/10.5382/econgeo.4911

Keays RR, Lightfoot PC (2010) Crustal sulfur is required to form magmatic Ni–Cu sulfide deposits: evidence from chalcophile element signatures of Siberian and Deccan Trap basalts. Miner Deposita 45:241–257

Kiseeva ES, Wood BJ (2013) A simple model for chalcophile element partitioning between sulphide and silicate liquids with geochemical applications. Earth Planet Sci Lett 383:68–81. https://doi.org/10.1016/j.epsl.2013.09.034

Kitakaze A, Machida T, Komatsu R (2016) Phase Relations in the Fe–ni–s System from 875 To 650 °c. Can Mineral 54:1175–1186. https://doi.org/10.3749/canmin.1500087

Kosyakov V, Sinyakova E (2012) Physicochemical prerequisites for the formation of primary orebody zoning at copper-nickel sulfide deposits (by the example of the systems Fe–Ni–S and Cu–Fe–S). Russ Geol Geophys 53:861–882

Latypov R (2015) Basal reversals in mafic sills and layered intrusions In: Charlier B, Namur O, Latypov R, Tegner C (eds) Layered Intrusions. Springer Netherlands, Dordrecht, pp 259–293

Le Vaillant M, Barnes SJ, Fiorentini ML, Miller J, McCuaig TC, Muccilli P (2015) A hydrothermal Ni-As-PGE geochemical halo around the Miitel Komatiite-Hosted nickel sulfide deposit, Yilgarn Craton, western Australia. Econ Geol 110:505–530

Lehmann J, Arndt N, Windley B, Zhou MF, Wang CY, Harris C (2007) Field relationships and geochemical constraints on the emplacement of the Jinchuan intrusion and its Ni-Cu-PGE sulfide deposit, Gansu, China. Econ Geol 102:75–94. https://doi.org/10.2113/gsecongeo.102.1.75

Lesher CM, Stone WE (1996) Exploration geochemistry of komatiites. In: Wyman DA (ed) Igneous trace elements geochemistry, application for massive sulphide exploration, geological association of Canada (Vol 12, pp 153–204). Short Course Notes, St. John's

Lesher CM, Burnham OM (2001) Multicomponent elemental and isotopic mixing in Ni-Cu-(PGE) ores at kambalda, Western Australia. Can Mineral 39:421–446. https://doi.org/10.2113/gscanmin.39.2.421

Lesher CM (2017) Roles of xenomelts, xenoliths, xenocrysts, xenovolatiles, residues, and skarns in the genesis, transport, and localization of magmatic Fe-Ni-Cu-PGE sulfides and chromite. Ore Geol Rev 90:465–484. https://doi.org/10.1016/j.oregeorev.2017.08.008

Lesher CM (2019) Up, down, or sideways: emplacement of magmatic Fe–Ni–Cu–PGE sulfide melts in large igneous provinces1. Can J Earth Sci 56:756–773. https://doi.org/10.1139/cjes-2018-0177

Li Y, Audétat A (2012) Partitioning of V, Mn Co, Ni, Cu, Zn, As, Mo, Ag, Sn, Sb, W, Au, Pb, and Bi between sulfide phases and hydrous basanite melt at upper mantle conditions. Earth Planet Sci Lett 355–356:327–340. https://doi.org/10.1016/j.epsl.2012.08.008

Li CS, Ripley EM (2005) Empirical equations to predict the sulfur content of mafic magmas at sulfide saturation and applications to magmatic sulfide deposits. Miner Deposita 40:218–230. https://doi.org/10.1007/s00126-005-0478-8

Li CS, Barnes SJ, Makovicky E, RoseHansen J, Makovicky M (1996) Partitioning of nickel, copper, iridium, rhenium, platinum, and palladium between monosulfide solid solution and sulfide liquid: effects of composition and temperature. Geochim Cosmochim Acta 60:1231–1238

Li CS, Xu ZH, de Waal SA, Ripley EM, Maier WD (2004) Compositional variations of olivine from the Jinchuan Ni-Cu sulfide deposit, western China: implications for ore genesis. Miner Deposita 39:159–172

Li XH, Su L, Chung SL, Li ZX, Liu Y, Song B, Liu DY (2005) Formation of the Jinchuan ultramafic intrusion and the world's third largest Ni-Cu sulfide deposit: Associated with the ~825 Ma south China mantle plume? Geochem Geophys Geosyst 6:1–6

Liang QL, Song XY, Wirth R, Chen LM, Dai ZH (2019) Implications of nano- and micrometer-size platinum-group element minerals in base metal sulfides of the Yangliuping Ni-Cu-PGE sulfide deposit, SW China. Chem Geol 517:7–21. https://doi.org/10.1016/j.chemgeo.2019.04.015

Liu Y, Brenan J (2015) Partitioning of platinum-group elements (PGE) and chalcogens (Se, Te, As, Sb, Bi) between monosulfide-solid solution (MSS), intermediate solid solution (ISS) and sulfide liquid at controlled fO2–fS2 conditions. Geochim Cosmochim Acta 159:139–161. https://doi.org/10.1016/j.gca.2015.03.021

Lu YG, Lesher CM, Deng J (2019) Geochemistry and genesis of magmatic Ni-Cu-(PGE) and PGE-(Cu)-(Ni) deposits in China. Ore Geol Rev 107:863–887

Maier WD, Barnes SJ, Chinyepi G, Barton JM, Eglington B, Setshedi I (2008) The composition of magmatic Ni-Cu-(PGE) sulfide deposits in the Tati and Selebi-Phikwe belts of eastern Botswana. Miner Deposita 43:37–60

Mansur ET, Barnes S-J, Duran CJ (2019) Textural and compositional evidence for the formation of pentlandite via peritectic reaction: Implications for the distribution of highly siderophile elements. Geology 47:351–354

Mansur ET, Barnes S-J, Duran CJ (2021) An overview of chalcophile element contents of pyrrhotite, pentlandite, chalcopyrite, and pyrite from magmatic Ni-Cu-PGE sulfide deposits. Miner Deposita 56:179–204

Mao YJ, Barnes SJ, Duan J, Qin KZ, Godel BM, Jiao JG (2018) Morphology and Particle Size Distribution of Olivines and Sulphides in the Jinchuan Ni-Cu Sulphide Deposit: Evidence for Sulphide Percolation in a Crystal Mush. J Petrol 59:1701–1729. https://doi.org/10.1093/petrology/egy077

Mavrogenes JA, O'Neill HSC (1999) The relative effects of pressure, temperature and oxygen fugacity on the solubility of sulfide in mafic magmas. Geochim Cosmochim Acta 63:1173–1180. https://doi.org/10.1016/S0016-7037(98)00289-0

Mungall JE (2002) Late-stage sulfide liquid mobility in the main mass of the Sudbury Igneous Complex: examples from the Victor Deep, McCreedy East, and Trillabelle deposits. Econ Geol 97:1563–1576

Mungall JE, Brenan JM (2014) Partitioning of platinum-group elements and Au between sulfide liquid and basalt and the origins of mantle-crust fractionation of the chalcophile elements. Geochim Cosmochim Acta 125:265–289

Mungall JE, Andrews DRA, Cabri LJ, Sylvester PJ, Tubrett M (2005) Partitioning of Cu, Ni, Au, and platinum-group elements between monosulfide solid solution and sulfide melt under controlled oxygen and sulfur fugacities. Geochim Cosmochim Acta 69:4349–4360. https://doi.org/10.1016/j.gca.2004.11.025

Pearce TH (1968) A contribution to the theory of variation diagrams. Contrib Miner Petrol 19:142–157

Prichard HM, Knight RD, Fisher PC, McDonald I, Zhou M-F, Wang CY (2013) Distribution of platinum-group elements in magmatic and altered ores in the Jinchuan intrusion, China: an example of selenium remobilization by postmagmatic fluids. Miner Deposita 48:767–786. https://doi.org/10.1007/s00126-013-0454-7

Puchtel IS, Humayun M (2001) Platinum group element fractionation in a komatiitic basalt lava lake. Geochim Cosmochim Acta 65:2979–2993

Qi L, Zhou M, Wang C (2004) Determination of low concentrations of platinum group elements in geological samples by ID-ICP-MS. J Anal at Spectrom 19:1335–1339

Qi L, Gao J, Huang X, Hu J, Zhou M-F, Zhong H (2011) An improved digestion technique for determination of platinum group elements in geological samples. J Anal at Spectrom 26:1900–1904

Righter K, Campbell AJ, Humayun M, Hervig RL (2004) Partitioning of Ru, Rh, Pd, Re, Ir, and Au between Cr-bearing spinel, olivine, pyroxene and silicate melts. Associate editor: C. R Neal Geochimica Et Cosmochimica Acta 68:867–880

Ripley EM, Li C (2003) Sulfur isotope exchange and metal enrichment in the formation of magmatic Cu-Ni-(PGE) deposits. Econ Geol 98:635–641

Ripley EM, Sarkar A, Li CS (2005) Mineralogic and stable isotope studies of hydrothermal alteration at the Jinchuan Ni-Cu deposit, China. Econ Geol 100:1349–1361

Savard D, Barnes SJ, Meisel T (2010) Comparison between nickel-sulfur fire assay Te Co-precipitation and isotope dilution with high-pressure asher acid digestion for the determination of platinum-group elements, rhenium and gold. Geostand Geoanal Res 34:281–291

Sixth Geological Unit (1984) Geology of the Baijiaozuizi Cu-Ni sulfide deposit. Geological Survey of Gansu Province, Geological publishing House, Beijing, Sixth Geological Unit

Song XY, Zhou MF, Wang CY, Qi L, Zhang CJ (2006) Role of crustal contamination in formation of the Jinchuan intrusion and its world-class Ni-Cu-(PGE) sulfide deposit, northwest China. Int Geol Rev 48:1113–1132

Song XY, Keays RR, Zhou MF, Qi L, IhIenfeld C, Xiao JF (2009) Siderophile and chalcophile elemental constraints on the origin of the Jinchuan Ni-Cu-(PGE) sulfide deposit, NW China. Geochim Cosmochim Acta 73:404–424

Song XY, Danyushevsky LV, Keays RR, Chen LM, Wang YS, Tian YL, Xiao JF (2012) Structural, lithological, and geochemical constraints on the dynamic magma plumbing system of the Jinchuan Ni-Cu sulfide deposit, NW China. Miner Deposita 47:277–297

Song XY, Wang KY, Barnes SJ, Yi JN, Chen LM, Schoneveld LE (2020) Petrogenetic insights from chromite in ultramafic cumulates of the Xiarihamu intrusion, northern Tibet Plateau, China. Am Miner 105:479–497

Stanley CR, Russell JK (1989) Petrologic hypothesis testing with Pearce element ratio diagrams: derivation of diagram axes. Contrib Miner Petrol 103:78–89

Su SG, Li CS, Zhou MF, Ripley EM, Qi L (2008) Controls on variations of platinum-group element concentrations in the sulfide ores of the Jinchuan Ni-Cu deposit, western China. Miner Deposita 43:609–622

Sullivan NA, Zajacz Z, Brenan JM, Hinde JC, Tsay A, Yin Y (2022a) The solubility of gold and palladium in magmatic brines: Implications for PGE enrichment in mafic-ultramafic and porphyry environments. Geochim Cosmochim Acta 316:230–252

Sullivan NA, Zajacz Z, Brenan JM, Tsay A (2022b) The solubility of platinum in magmatic brines: Insights into the mobility of PGE in ore-forming environments. Geochim Cosmochim Acta 316:253–272. https://doi.org/10.1016/j.gca.2021.09.014

Tang ZL, Li WY (1995) Mineralization model and geology of the Jinchuan deposit bearing PGE. Geological Publishing House (in Chinese), Beijing

Tang ZL (1991) Formation of the Jinchuan Cu–Ni sulfide deposit. Modern Geol (in Chinese) 4:55–64

Tonnelier NJ (2010) Geology and genesis of the Jinchuan Ni-Cu-(PGE) deposit, China: Unpublished Ph.D. thesis, Sudbury, Canada, Laurentian University, pp 1–192

Waal SD, Xu Z, Li C, Mouri H (2004) Emplacement of viscous mushes in the Jinchuan ultramafic intrusion, western China. Can Mineral 42:371–392

Waldner P, Pelton AD (2004) Critical thermodynamic assessment and modeling of the Fe-Ni-S system. Metall and Mater Trans B 35:897–907. https://doi.org/10.1007/s11663-004-0084-7

Xie W, Song XY, Chen LM, Deng YF, Zheng WQ, Wang YS, Ba DH, Yin MH, Luan Y (2014) Geochemistry insights on the genesis of the subduction-related Heishan magmatic Ni-Cu-(PGE) deposit, Gansu, northwestern China, at the Southern Margin of the Central Asian Orogenic Belt. Econ Geol 109:1563–1583

Yang S, Qu W, Tian Y, Chen J, Yang G, Du A (2008) Origin of the inconsistent apparent Re–Os ages of the Jinchuan Ni–Cu sulfide ore deposit, China: Post-segregation diffusion of Os. Chem Geol 247:401–418

Zhang M, Kamo SL, Li C, Hu P, Ripley EM (2010) Precise U-Pb zircon–baddeleyite age of the Jinchuan sulfide ore-bearing ultramafic intrusion, western China. Miner Deposita 45:3–9